Simulation of the Position Resolution of a Scintillation Detector

BACHELORARBEIT

Stefan-Meyer-Institut (SMI)
Österreichische Akademie der Wissenschaften (ÖAW)

vorgelegt am: 8. Oktober 2014

Name:	Sebastian Templ
Matrikelnummer:	1125396
Universität:	Technische Universität Wien
Studiengang:	Technische Physik (033 261)
Beurteilung:	Privatdoz. Dipl.-Ing. Dr. Johann Marton
Betreuung:	Dipl.-Ing. Clemens Sauerzopf

Kurzfassung

Dem Standardmodell der Teilchenphysik zufolge ist die CPT-Symmetrie fundamental. Um diese Vorhersage zu testen, entwickelt die ASACUSA-Kollaboration ("Atomic Spectroscopy And Collisions Using Slow Antiprotons") ein Rabi-ähnliches Experiment zur präzisen Messung der Hyperfeinstruktur von Antiwasserstoff. Der Vergleich der experimentell ermittelten Antiwasserstoff-Übergangsfrequenzen mit jenen des Wasserstoffs erlaubt einen direkten Test der CPT-Symmetrie.

Das Spektrometer im HBAR-GSHFS-Experiment ("Antihydrogen ground state hyperfine splitting") der Kollaboration besteht aus einer Teilchenquelle, einer Mikrowellenkavität zur Induktion von Spin-Flips, einem Sextupolmagneten zur Analyse der Teilchenspins und einem Detektor.

Im Laufe dieser Arbeit wurde ein Szintillationsdetektor, wie er im Hodoskop des Detektors am Ende des Spektrometeraufbaus eingesetzt wird, mit dem Teilchenphysik-Toolkit Geant4 [1, 2] simuliert. Eine nachfolgende Analyse der Simulationsdaten erlaubt eine Abschätzung der minimalen Unbestimmtheit in der Identifikation jener Punkte, an denen die zu detektierenden Teilchen auf die Detektorgeometrie treffen.

Abstract

In the Standard Model of particle physics, CPT symmetry is regarded as invariant. In order to test this prediction, the ASACUSA collaboration ("Atomic Spectroscopy And Collisions Using Slow Antiprotons") aims to make a very precise measurement of the hyperfine structure of antihydrogen with a Rabi-like experiment. The comparison of the experimentally-obtained antihydrogen transition frequencies with those of hydrogen allows for a direct test of CPT symmetry.

The spectrometer line of the ASACUSA HBAR-GSHFS ("Antihydrogen ground state hyperfine splitting") experiment consists of a particle source, a spin flip-inducing microwave cavity, a spin-analyzing sextupole magnet, and a detector.

In the course of the work for this thesis, a single scintillation detector as used in the hodoscopes of the detector at the end of the spectrometer line was simulated using the particle physics toolkit Geant4 [1, 2]. Subsequent analysis of the simulation data allows for an estimate of the minimal uncertainty in determining the location of a particle's point of impact on the detector geometry.

Contents

Chapter 1

Introduction

The hydrogen atom has always been one of physicists' favorite systems as it is the simplest atomic composition occurring naturally and in vast amounts in the universe. Thus it is not surprising that hydrogen is one of the best-known physical systems.

The Bohr model [3] was one of the first concepts capable of satisfyingly describing a wide range of observations concerning the atomic structure of hydrogen. However, some of its basic assumptions were questionable and several phenomena were not able to be explained by it. A huge step forward was made when the atomic building blocks of nature could finally be described in terms of quantum mechanics. As it turned out, this newly established theoretical framework even allowed for a perfect description of the hydrogen atom. The study of this simplest atom has always been a fruitful endeavour as it reveals fundamental insights into our physical world.

One of those revolutionary insights was the postulation of antimatter by Paul Dirac in 1928 [4] and its experimental confirmation by Carl David Anderson soon after in 1932 [5]. Accordingly, for each species of particle there exists a mirror-charged version, i.e. its antiparticle.

The existence of antimatter, among other concepts and discoveries, made for the formulation of relations between transformations of charge (C), parity (P), and time (T). Fundamental symmetries were looked for which leave a physical process unchanged after the transformation of combinations of these quantities.

Remarkably, neither C nor P are fully conserved in the weak interaction. A simple example for this is the production of a neutrino in an accelerator which always results in this particle having a left-handed spin or, in other words, a negative helicity. The same characteristics apply to the production of an antineutrino with a positive helicity. A combined C and P transformation, though, yields a type of particle actually observable in nature. Therefore, for a long period of time, CP was considered as never being violated. However, in 1964 the CP violation was first discovered in neutral kaons [6] and later on in several other systems.

The symmetry of CPT, as formulated in a theorem by Lüders and Pauli [7, 8], is still considered to be an exact one even on a fundamental level and is deeply intertwined into the theoretical frameworks of modern theories. A violation of CPT would have striking consequences for our understanding of the physical world as it would automatically invoke a Lorentz violation [9]. Until now there are no convincing experimental results that indicate a CPT violation though.

A promising and direct test of CPT is the study of the hyperfine structure of antihydrogen. Experimental results of such an experiment can be compared to observations of hydrogen since the latter is a well-known physical system, as already pointed out above. The ASACUSA collaboration aims at realizing such an experiment.

This thesis is only a small contribution to a much larger project, but hopefully it will be of help in gathering new knowledge about our world.

Chapter 2

Theoretical Background

2.1 The Hyperfine Structure of Hydrogen

The hyperfine structure is the result of the electromagnetic interaction between the total angular momentum of the electron $\vec{J}$ and the one of the nucleus $\vec{I}$, with the atomic total angular momentum being $\vec{F} = \vec{J} + \vec{I}$.

In hydrogen, the hyperfine interaction causes the splitting of the ground state into a *singlet* ($F = 0$) and a *triplet* ($F = 1$) state, where the former is non-degenerate and the latter has a threefold degeneracy (see figure 2.1).

The transition frequency ν_{HF} between these two energy levels without an external magnetic field is one of the most accurately measured physical quantities [10, 11].

$$\nu_{\mathrm{HF}} = 1\,420\,405\,751.7667 \pm 0.0009 \text{ Hz}. \tag{2.1.1}$$

Applying an external magnetic field to the hydrogen atom not only results in a shifting of all states but also in the splitting of the degenerate ($F = 1$) level into three distinguishable states. Now, instead of only one, several different transitions are observable, as figure 2.2 indicates.

Further, atoms with $(F, M_F) \in \{(1,1),(0,0)\}$ align parallel and atoms with $(F, M_F) \in \{(1,-1),(1,0)\}$ align antiparallel with respect to the magnetic field in order to reduce their total energy. If the external field is an inhomogeneous one (i.e., a field gradient exists), the atoms will move towards higher field densities if they are in one of the parallel states, or towards lower ones if they are aligned antiparallel. Therefore it seems natural to label them as *high field seeking* (HFS) and *low field seeking* (LFS) states, respectively.

It should however be noted that the order of HFS and LFS states is different for hydrogen and antihydrogen. Table 2.1 gives an overview.

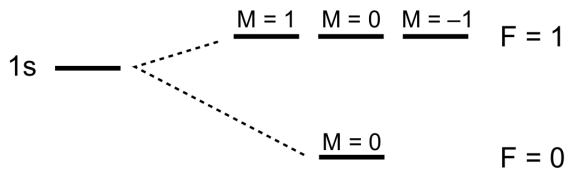

Figure 2.1: Hyperfine splitting of the hydrogen's ground state due to the electron and proton spin interaction.

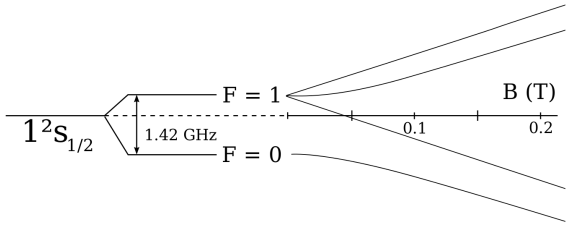

Figure 2.2: Hyperfine splitting and Breit-Rabi diagram. Splitting of the hyperfine levels in an external magnetic field.

	HFS states	LFS states
H	$(1,-1)$, $(0,0)$	$(1,1)$, $(1,0)$
$\overline{\text{H}}$	$(1,1)$, $(0,0)$	$(1,-1)$, $(1,0)$

Table 2.1: Overview of HFS and LFS states in hydrogen and antihydrogen [12].

2.2 CPT Symmetry

Apart from continuous symmetries, which lead to the conservation laws of physics according to Noether's theorem [13], there are three discrete symmetries playing an essential role in particle physics. Abbreviated with C, P and T, respectively, the relations between charge, parity and time were combined into the CPT theorem by Gerhart Lüders and Wolfgang Pauli [7, 8]. This theorem states that the discrete symmetry of CPT is an exact one, or – in other words – that any physical process remains the same when having a reversed charge (i.e., an exchange of matter and antimatter) and being reflected in space (parity) and time. Thus, the properties of matter and antimatter must be identical (mass, lifetime) or equal but opposite (charge, magnetic moment) under CPT transformation. Figure 2.3 illustrates both the CP and the CPT symmetry.

In particular, the CPT theorem also results in atoms and their antiparticles both being expected to have the same characteristic spectrum.

If any deviation from this symmetry could be found experimentally, it would hint at physical effects originating from a more fundamental theory beyond the Standard Model of particle physics [14].

A possible way to test CPT symmetry is the hyperfine spectroscopy of antihydrogen with a precision comparable to the case of hydrogen, since the hyperfine transition frequency of hydrogen is already one of the best known properties of matter (up to a precision of 10^{-12} [15]).

2.3 Scintillation Detectors

2.3.1 Basic Operation Principle

A scintillator is a material that, when struck by an incoming particle (i.e., ionizing radiation), re-emits the absorbed particle energy in the form of light. The whole point of this kind of material is the production of a large light output in the visible range (or in the most sensitive range of a light sensor) for particle detection purposes.

When a scintillator is coupled to an electronic light sensor such as a silicon photomultiplier (SiPM), a "scintillation detector" – or sometimes also referred to

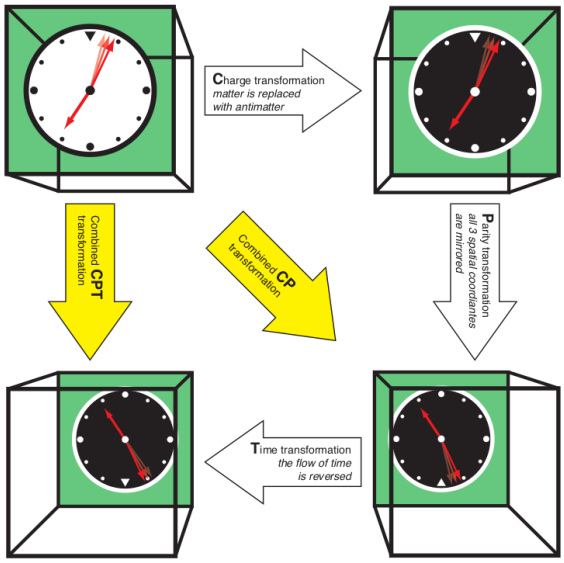

Figure 2.3: Illustration of the CP and the CPT symmetry (chart by Bertalan Juhász).

as a "scintillation counter" – is obtained: The light produced in the scintillating material arrives at the sensor where its energy is converted into electronic signals which can be used to reconstruct information about the particle that initially hit the scintillator.

2.3.2 Inorganic Scintillators and Their Electronic Band Structure

The energetic conditions of electrons in a pure inorganic crystal lattice can be modelled in terms of energy "bands". At it, the gap between the (lower) *valence band* and the (higher) *conduction band* represents the amount of energy necessary to elevate an electron from the ground state to an excited state. The space between the bands can never be accessed by electrons. Figure 2.4 shows the electronic band structures of different materials.

Once an electron has been excited into the conduction band, it seeks to "fall" down into the valence band again in order to reduce its energy. However, de-excitation via the emission of a photon is an inefficient process and so the energy is mostly emitted by other mechanisms. Besides, the width of the band gap in a pure crystal corresponds to an energy resulting in an emitted photon being in the

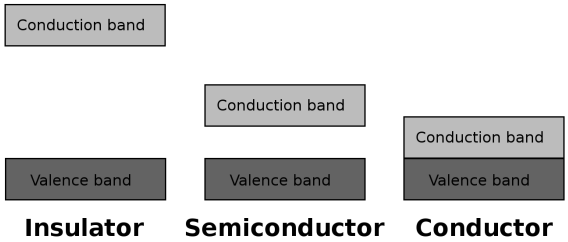

Figure 2.4: Schematic representation of the energy band structure of insulators, semiconductors, and conductors. The gap between the bands corresponds to the energy necessary to elevate an electron from the valence to the conduction band.

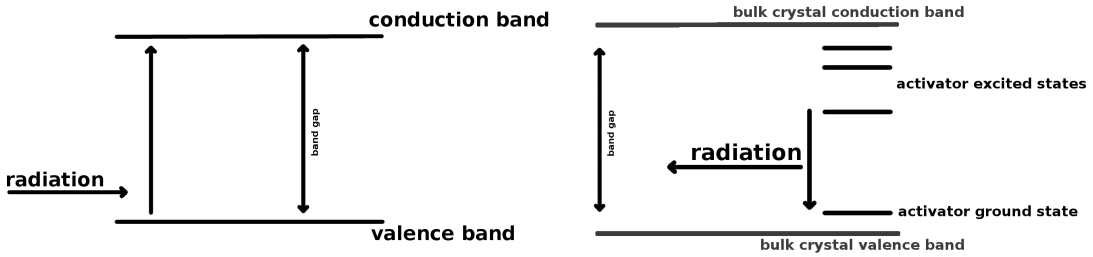

(a) pure crystal (b) activated scintillator

Figure 2.5: Energy band structure of an inorganic scintillator.

ultraviolet – hence not in the visible – range of the electromagnetic spectrum.

In order to produce scintillators with properties more suitable for practical purposes (i.e, a high yield of light in the visible range), small impurities are introduced into the scintillator material. These impurities, being foreign atoms in trace amounts, alter the energetic conditions in the scintillator's atomic lattice and therefore create sites with a different local band structure while the overall energy structure of the crystal remains unchanged. In particular, the impurities, which are also called *activators*, result in many sites having electron-accessible energy levels in the otherwise-forbidden band gap (see figure 2.5). Electrons in the conduction band can therefore de-excite via these levels.

Since the gap between the valence and the conduction band is narrower in the presence of an activator, an electron falling back into its ground state at this very location results in an emitted photon having a lower energy than the "normal" energy equivalent of a typical lattice band gap. Thus, for so-emitted photons, the scintillator material is practically invisible, because the excitation of further electrons only works at higher energy scales being non-accessible to them. Such photons are also referred to as *optical photons*.

When a particle or ionizing radiation hits the scintillator, lots of electron-hole pairs are produced. The positively charged hole quickly drifts to the location of an activator, which is ionized in this process. The ionization happens mainly at activator sites since the ionization energy of the impurity atoms is lower than the one of the atoms in the bulk lattice.

The excited electron in the conduction band, however, freely propagates through the crystal – at least until it comes upon an ionized activator site. Then the previously ionized impurity atom, together with the electron, forms a neutral configuration with the electron still being in an excited state at first. What follows is the electron transition to the ground state with a high probability of photon emission.

By carefully choosing the type of activator, an emission of optical photons in either the visible range or in the sensitive range of a detector can be achieved.

2.3.3 Silicon Photomultipliers (SiPMs)

A Silicon photomultiplier (SiPM) is a device specifically designed to detect single photon events by converting the photon energy into an analyzable electronic signal.

Its key component is an array of avalanche photodiodes (APD), each being a highly sensitive semiconductor device that converts light into digital signals by making use of the photoelectric effect. In a way, APDs can be considered the semicon-

ductor analog to photomultipliers, at least from a functional point of view.

APDs in a SiPM operate in Geiger-mode which means that an incoming photon triggers the avalanche current of a reverse biased p-n junction. Therefore, the APDs are specifically designed to operate well above the breakdown voltage of the p-n diodes. The microcells are read in parallel and enable the SiPM to generate signals within a dynamic range from a single photon to thousands of photons while a much lower supply voltage than in the case of traditional photomultiplier tubes is sufficient.

Photographs of the SiPM as used in the actual experiment can be seen in figure 3.7.

Chapter 3

Experimental Setup

3.1 The Rabi Experiment

The ASACUSA[1] experiment builds on an experiment first proposed by I. Rabi in 1938, which was the first application of the magnetic resonance principle for determining the hyperfine structure of hydrogen.

However, the ASACUSA collaboration aims at measuring the *anti*hydrogen's hyperfine structure.

In the original Rabi experiment the atomic beam first passes an inhomogeneous magnetic field region where a spin state is selected. The same mechanism, as has already been exploited by O. Stern and W. Gerlach in 1922 [17], is being used. Thereafter, the beam enters a region of a radiofrequency field superimposed with a homogeneous magnetic field. If the oscillating field induces a spin flip (an occurence strongly dependent on the field's frequency), the beam gets deflected by a posterior magnetic field gradient or otherwise focused towards the detector. While the frequency of the oscillating field is being kept constant, the force of the superimposed homogeneous magnetic field is varied. By subsequently counting the hits in the detector, the transition frequencies of the atoms in the beam can be determined very precisely.

However, in the ASACUSA setup, the resonance spectra in the detector will have a double peak structure as a result of the field distribution in the microwave chamber. Since the standing wave inside the cavity can be thought of as two waves – one traveling in beam direction and the other conversely – the double peak feature of the spectrum can be considered a Doppler splitting [18]. Therefore, the extent

[1] ASACUSA stands for "Atomic Spectroscopy And Collisions Using Slow Antiprotons".

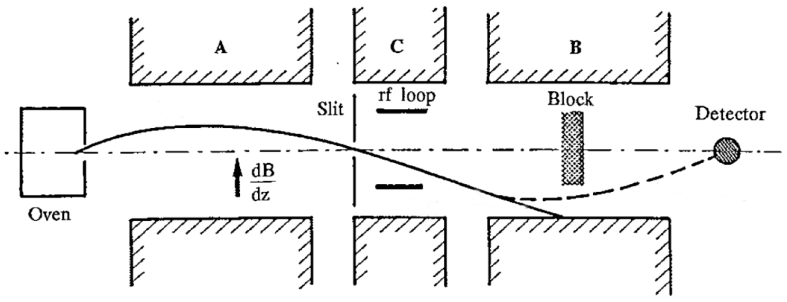

Figure 3.1: Setup of the Rabi experiment [16].

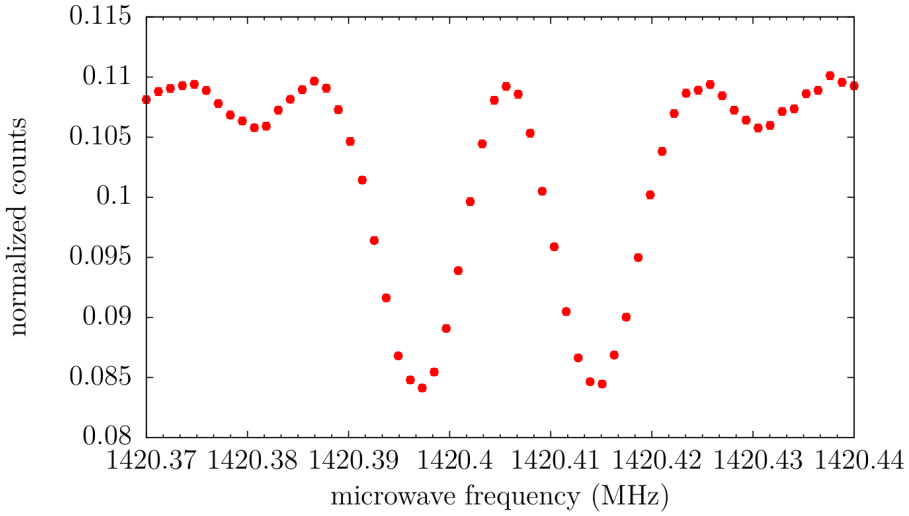

Figure 3.2: Typical resonance spectrum (simulated): Transition at zero magnetic field using 10^6 monoenergetic (0.01 eV) antihydrogen atoms per scan point. 70% LFS and 30% HFS states. [12]

of the splitting is proportional to the velocity of the beam and the exact shape of the spectrum depends on the velocity distribution within the beam (monovelocitic / Maxwell-Boltzmann-distributed).

A typical resonance spectrum as produced by the ASACUSA setup can be seen in figure 3.2.

3.2 The ASACUSA Experiment

The purpose of the HBAR-GSHFS[2] experimental setup used by the ASACUSA collaboration, as schematically depicted in figure 3.3 (for technical drawings of the beamline setup, see appendix A.2), is the testing of the CPT symmetry by measuring the ground state hyperfine structure of antihydrogen. Similarities to the Rabi setup can be clearly recognized.

[2] "Antihydrogen ground state hyperfine splitting"

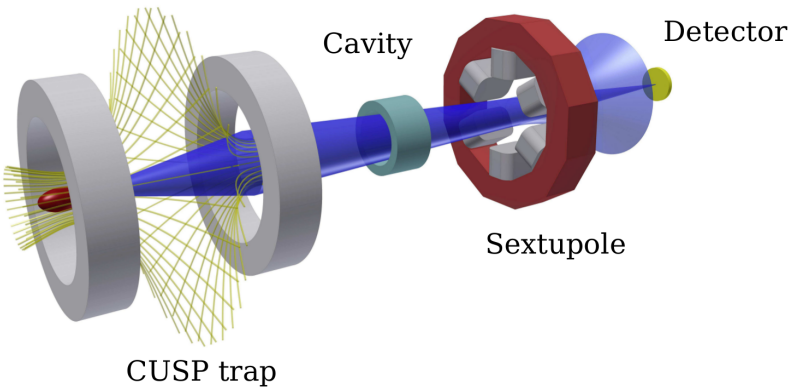

Figure 3.3: The experiment as a schematic drawing.

There are four main stages forming the setup:

1. A CUSP trap for assembling antihydrogen atoms from positrons and antiprotons.
2. A microwave cavity in which the hyperfine transitions are induced.
3. A sextupole magnet for selecting spin states by either deflecting or focusing the beam.
4. A detector specifically designed to detect antihydrogen events.

The building blocks of antihydrogen, i.e. positrons and antiprotons, are respectively produced by a ^{22}Na source via β^+ decay and by the Proton Synchrotron (PS) beam which is extracted onto an Iridium target with a momentum of 3.5 GeV/c for this purpose. Afterwards, for experimental use, the antiprotons are stored and decelerated down to an energy of 100 MeV/c by the Antiproton Decelerator (AD). They are further decelerated to 20-120 keV by the ASACUSA RFQD[3] in order to store them in Penning traps before they are injected into the CUSP trap where the actual synthesis of a spin-polarized antihydrogen beam happens.

For further information on the CUSP trap see [19, 20].

The microwave cavity holds an oscillating magnetic field which induces the spin flips and a superimposed homogeneous magnetic field which is varied in the course of the experiment in order to shift the hyperfine levels of antihydrogen and determine its characteristic spectrum.

The cavity field is very homogeneuous in the plane orthogonal to the beam and has a sinusoidal distribution in beam direction.

In the center of the cavity the field is zero and it has maxima at the beam's entrance and exit point. Hence, the frequency scan has a double peak structure: When the field oscillation rate is on resonance with the transition frequency of the respective atoms, the signal is zero for the two regions' effects cancelling each other (see again figure 3.4).

The cavity in the ASACUSA setup allows for two transitions called σ_1 and π_1 (see figure 3.5). In order to choose a particular transition the relative alignment between the oscillating and the static magnetic field has to be adjusted. (For the σ_1 transition to take place the two fields must be parallel and for the π_1 transition they must be orthogonal.)

Since, for small field intensities, the σ_1 transition is less sensitive to inhomogeneities of the external field, due to its second order field dependence, than the linearly behaving π_1, measuring this transition is currently preferred, although it is believed to be necessary to also investigate the π_1 transition in following experiments in order to probe for an eventual CPT violation. By measuring the resonance frequencies of the σ_1 transition for different external field intensities, an extrapolation to the zero-field case can be performed in order to determine the undisturbed hyperfine structure of antihydrogen.

Finally, at the end of the spectrometer line, a detector is placed. This device, called Compact Pion Tracking Detector (or, appositely, CPT detector), consists of

[3] "RadioFrequency Quadrupole Decelerator"

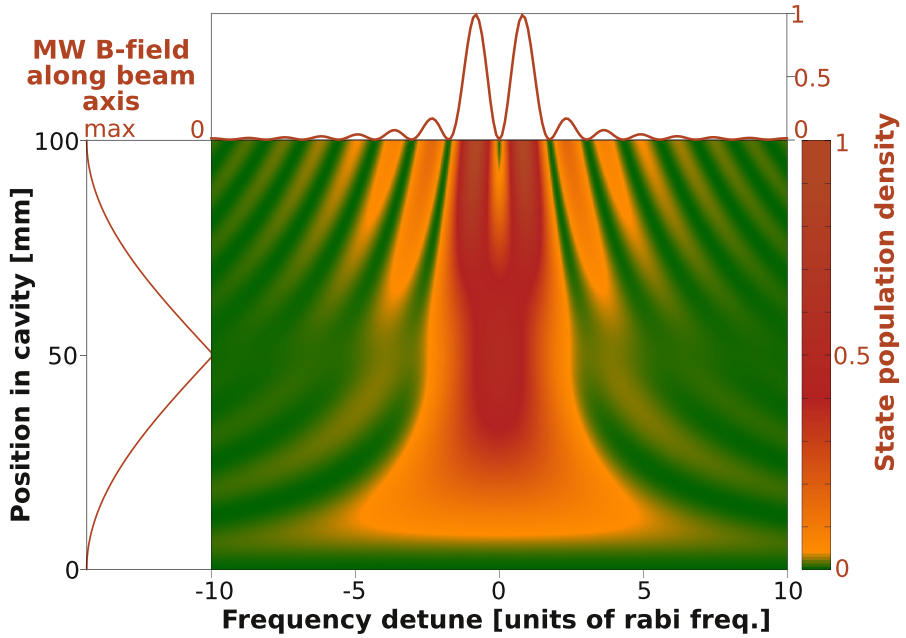

Figure 3.4: Distribution of the state population density within the microwave cavity (simulated). Transition-inducing effects on spins that pass through the cavity center net to zero due to the "orientation-switching" B-field distribution along the beam axis.

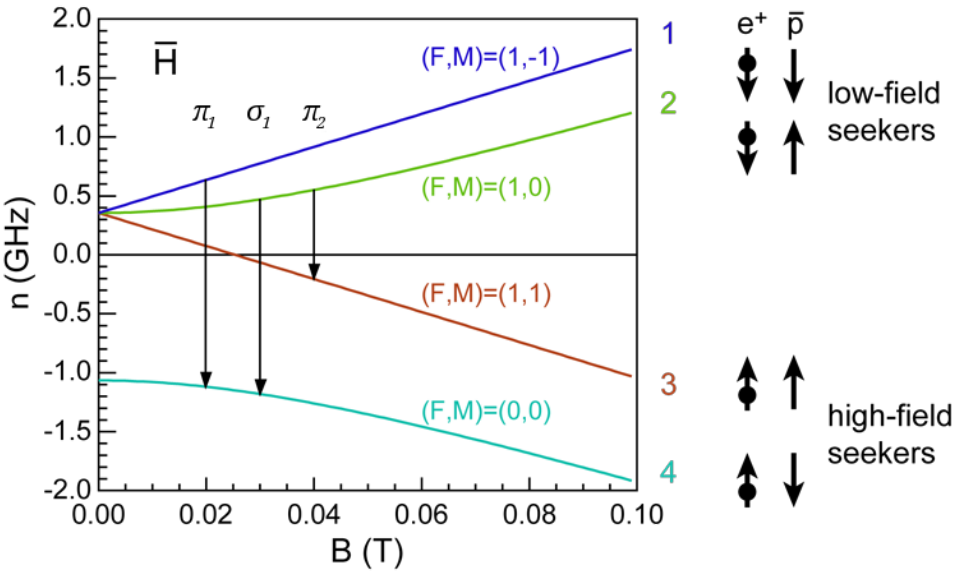

Figure 3.5: Breit-Rabi diagram of the hyperfine splitting in an external magnetic field with suitable transitions for a spin state analyzing experiment.

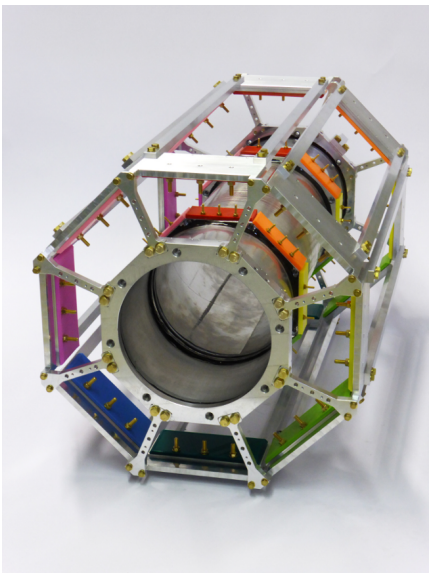

(a) The hodoscope scaffold.

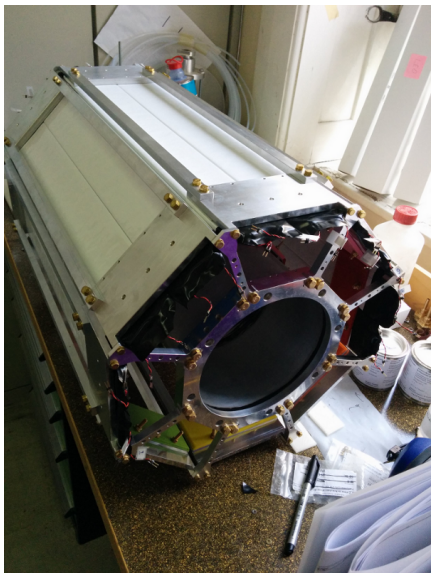

(b) Construction of the hodoscope with a layer of scintillation detectors already mounted (white).

Figure 3.6: The hodoscope of the CPT detector.

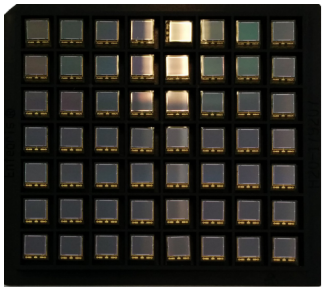

(a) A fraction of the SiPMs as they were shipped.

(b) A pair of SiPMs before being mounted on the end of a scintillator.

Figure 3.7: The Silicon Photo Multipliers (SiPM)

a central BGO (bismuth germanate) detector and a two-layered hodoscope of scintillation counters (see figure 3.6). An incoming antihydrogen atom collides with the BGO and produces mainly pions which deposit energy in the BGO as well as in the hodoscope. There, in the scintillators of the hodoscope, the optical photons produced in the scintillating material are directed towards the ends of the scintillator bar where they are converted into electrical signals by SiPMs (Silicon PhotoMultipliers, see figure 3.7).

Figure 3.8 shows a scintillator-lightguide assembly before the mounting of the SiPMs and the wrapping with aluminium foil. A scintillation detector ready to be integrated into the experiment can be seen in figure 3.9.

It is important to establish a high detection efficiency in the CPT Detector since the antihydrogen production rate is much lower than in hydrogen experiments and also lower than the rate at which cosmic rays inevitably pass through the detector area.

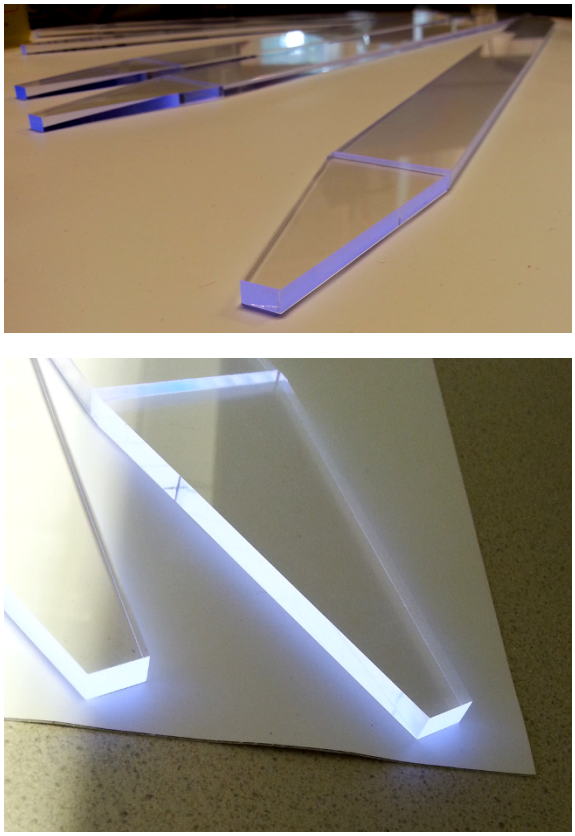

Figure 3.8: Scintillator bars with light guides as they were shipped. One can clearly see the purplish glow at the ends of the assembly as a result of the scintillation processes within the material even under normal room conditions.

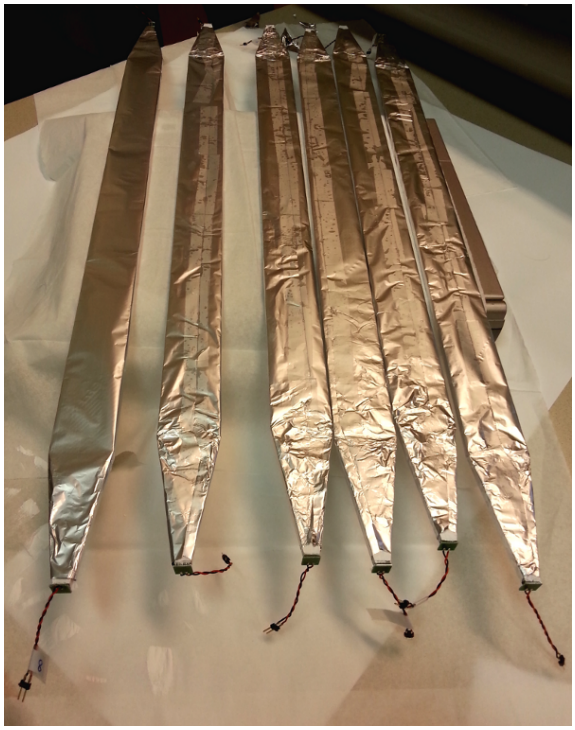

Figure 3.9: Scintillation detectors, ready to be built into the experiment.
The assembly in figure 3.8 has been expanded by the SiPM boards depicted in figure 3.7 (b) and an aluminium wrapping.

Chapter 4

Simulation of a Scintillation Detector

One of the major components of the CPT detector are the scintillation detectors. Each consists of a scintillating bar and trapezoid-shaped light guides with pairs of SiPMs at each end. Additionally, the whole device is surrounded by an aluminium wrapping.

When a particle hits the scintillator, the material produces optical photons which spread out in the material (see section 2.3.2). The majority of them undergo total inner reflection due to the relative refractive indices of the scintillator and the surrounding material. Photons which do escape the scintillator are reflected by the aluminium wrapping. This way, it is guaranteed that as many optical photons as possible are directed towards the ends of the scintillator where they hit the SiPMs and can be counted as electronic pulses.

The amount of detected optical photons depends on properties of the initial particle hit such as particle type and energy. By observing the optical photons' arrival time at each pair of SiPMs, it is possible to reconstruct the location of the original particle hit and finally identify antihydrogen events.

Knowing how optical photons behave in the particular type of scintillation detectors used in the ASACUSA setup presents a crucial point in the understanding of the physical processes happening in the CPT detector. It enables the important distinction between antihydrogen atoms annihilating in the detector and cosmic rays passing through the apparatus with energies comparable to the ones of the particles produced via the matter-antimatter annihilation.

Therefore it is natural to simulate the physical processes happening in a scintillation detector and compare these to experimental results.

In this chapter, it will be described how a suitable simulation was programmed, run, and interpreted. The framework used for programming is the Geant4[1] particle physics toolkit [1, 2] which was developed at CERN and is written in C++.

[1] "**Ge**ometry **an**d **t**racking"

4.1 Constructing the Geometry

4.1.1 Creating a GDML File

It is preferred to define and store the whole geometry of the simulation in a single GDML[2] file [21] not only for reasons of simplicity but also for application-independent usage due to its XML-based file format and easier analysis using the ROOT Data Analysis Framework [22].

Originally, it was intended to use technical drawings of the scintillation detector geometry in STL file format and converting them into GDML format using CADMesh [23]. However, it was observed that the simulation produces unphysical results when being run with an implementation of the CADMesh-converted GDML files. (In particular, the instantiation of the `G4Step` class is called only one in ten times.) The bug is suspected to be in the *tessellated solid navigation technique* [24] of CADMesh. A further investigation of it was not taken though.

Instead, the geometry was created with a seperate Geant4 code and then exported into a GDML file using Geant4's own `G4GDMLParser` class.

A visualization of the geometry as produced by Geant4 can be found in figure 4.1. The upper end of the scintillator bar (blue), the trapezoid-shaped light guide (white), and the pair of SiPMs on top of it (yellow) can be clearly recognized. One might need a closer look to spot the aluminium wrapping surrounding both the bar and the light guide since it is only 16 μm thick and 0.5 mm apart from the inner geometry.

The physical dimensions of the detector are taken from a technical drawing, which is appended in A.1.

It should be noted for the following subchapters that the coordinate system used in the simulation has its origin in the center of the geometry with the positive y-axis pointing towards the top and the negative y-axis towards the bottom SiPM end. The beam direction is the positive z-axis while the larger scintillator surfaces are parallel to the plane orthogonal to the beam.

4.2 Definition of Materials

The components of the detector are placed within a world volume filled with air.

The base material for the BC-408 plastic scintillator is polyvinyl toluene and its density was set to 1.032 g/mole with the atomic ratio of hydrogen to carbon being 1.1 [25].

For the material of the light guides, the same atomic composition as for the scintillating material was chosen, the only difference being that the scintillation properties are set for the bar but not for the light guides. As a justification for that, it should be pointed out that mainly the respective refractive indices (see 4.2.1) between the two materials are relevant for the purposes of this simulation and not so much the exact atomic composition.

The SiPM material is plain silicon and the wrapping material aluminium.

The exact material definitions as used within the Geant4 framework of the simulation are quoted in appendix C.1.

[2] "Geometry Description Mark-up Language"

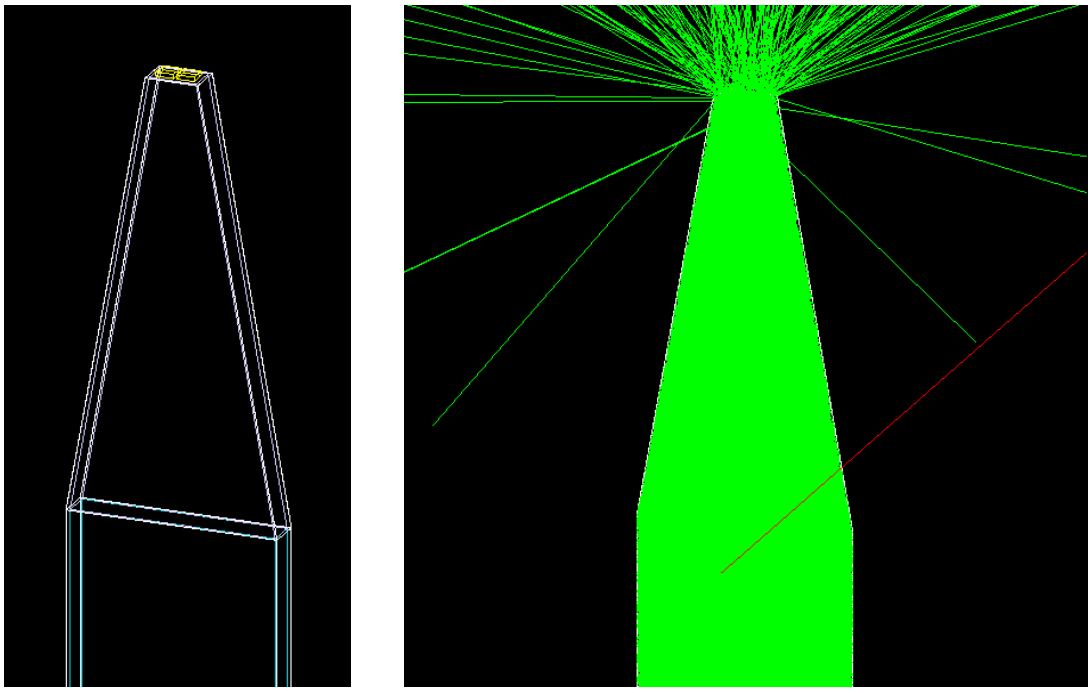

(a) no particle hit

(b) particle hit in the upper region of the scintillator (red: particle track, green: photons)

Figure 4.1: Visualization of the geometry as drawn by Geant4.
The picture shows just the upper part of the scintillation detector, but contains all the interesting features since the construction is symmetrical.

Material	Refractive index
Air	1.00027717
Plastic scintillator	1.58 (taken from the datasheet [25])
Light guide	1.58
SiPM	1.58

Table 4.1: Refractive indices as used in the simulation.

4.2.1 Material Properties and Optical Physics

First of all, the refractive indices of all materials have had to be defined. The used values[3] can be found in table 4.1.

The refractive index of the wrapping material is calculated by Geant4. For this purpose, the real and the imaginary part of the reflective index depending on the wavelength has to be fed into the program using `G4MaterialPropertiesTable` and an instance of `G4OpticalSurface` must be equipped with this properties table. The actual data for both indices is obtained from the literature (see B.1, [26]).

In order to provide the scintillation properties of the bar material, an instantiation of `G4OpticalPhysics` must be registered in the *physics list*. Only then do material properties concerning optical processes take effect.

It is also necessary to add the property of an absorption length to the scintillator

[3]Since the main purpose of the simulation is the evaluation of the number of optical photons hitting the SiPMs and their arrival times, it is reasonable to set the same refractive index for the SiPM and the light guide material.

Scintillation fast component	*read from data file, see B.2* [25]
Scintillation yield	10 000/MeV
Resolution scale	1
Fast time constant	1 ns
Absorption length	380 cm (taken from datasheet [25])

Table 4.2: Further parameters for the scintillator material.

material in order to produce physically meaningful data and prevent the simulation from running for unreasonably long times.

Some more relevant paramters are listed in table 4.2.

See C.2 for how the optical properties were implemented.

4.3 Sensitive Detectors

The *sensitive* parts of the geometry are the SiPMs.

Although actually consisting of two physically separate detection areas, each pair of SiPMs is treated as a single unit. Hence, in the following, they are to be labelled just as "top SiPM" and "bottom SiPM", meaning the upper and the lower pair of SiPMs, respectively, since the whole scintillation detector has a vertical alignment in the simulation (c.f. figure 4.1).

As soon as a particle track fully enters a sensitive detector volume, the current (global) time is ascertained and temporarily stored. Thereafter, the particle is of no further interest and thus its track is killed. At the end of a run the collected time data from each the top and the bottom SiPM is written into files and saved for later analysis.

See C.3 for code snippets concerning the sensitive detectors.

4.4 Running the Simulation

In order to produce simulation data a monoenergetic beam of negatively charged pions was fired at the scintillator perpedicular to the material surface. The pions' energy was set to 330.8774 MeV since this is their most probable energy expected.

Subsequently, a bash script was used to run the simulation repeatedly while controlling the position of the particle gun. In doing so, the scintillator bar was rastered with particle hits "from bottom to top" (i.e., along its y-axis, see 4.1.1) – 200 particles were fired at it every 0.1 mm.

Finally a full screen with 90 000 initial particle hits was obtained and data files containing the arrival times of optical photons at each of the SiPM pairs were stored for following analysis.

4.5 Analysis of Optical Photon Arrival Times

An additional C++ program was written in order to analyze the simulation data. The purpose of the analysis is to compute several average data values from 200 respective particle hits for each point on the scintillator bar. It should bring forth

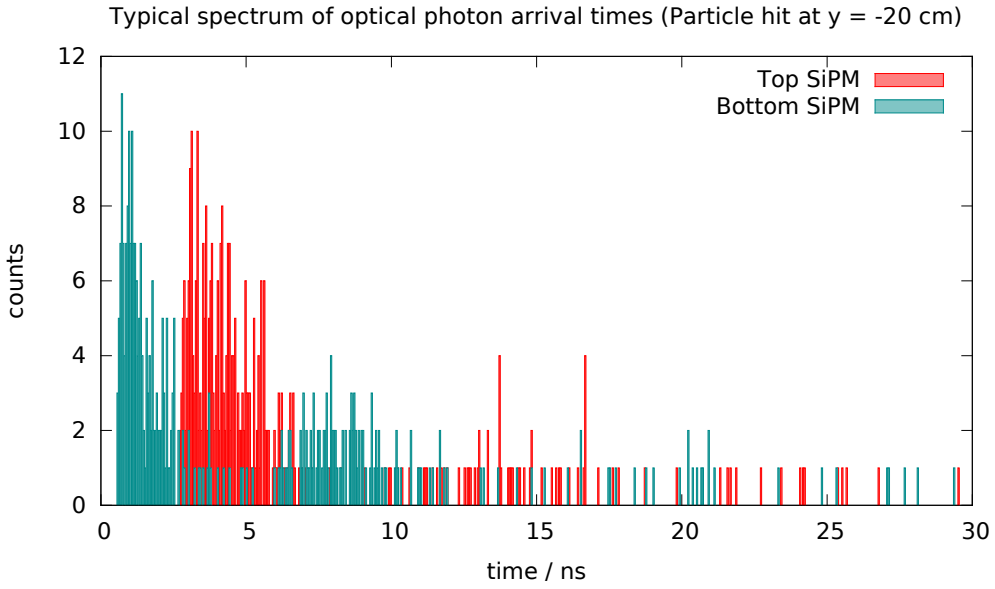

Figure 4.2: Typical spectrum of optical photon arrival times at each SiPM as produced by a single particle hit near the bottom end of the scintillator. The counts in the bottom SiPM can be clearly identified to happen earlier than the ones in the top SiPM. (The location statement of the hit is reduced to the y-coordinate since all particles hit the scintillator along the y-axis. This goes for all the following locations.)

predictions on the ideal position resolution of the particular kind of scintillation detector used in the ASACUSA experiment.

One by one, the files which were produced in the course of the simulation run were read and their optical photon arrival time data temporarily stored. In order to generate a meaningful time spectrum, the arrival times were converted into histograms. Thereby, the time resolution (i.e., the box width) was set to 200 picoseconds, in accordance with the actual data aquisition hardware which has a sampling frequency of 5 GHz and therefore a binwidth of 200 ps. The peak in each of these histograms indicates the time of the most photons arriving in a SiPM. An arbitrarily chosen typical time spectrum produced by a single particle hit is depicted in figure 4.2. Although not relevant for the actual data analysis, it might be interesting to point out that the significantly smaller local maxima following the main peak are photons having been reflected at the opposite side of the scintillation detector due to the inwards-bent sides of a light guide. The amount of such "reflected" photons is much smaller than the one of "directly" incoming ones for reasons of the detector geometry and photon absorption in the material.

The time of the most photons arriving at a SiPM is indicated by the peak in each histogram curve, as mentioned above. However, the peak is not a very realiable measure for the first photonic flush arriving at an end of the detector since its exact point of time varies relatively strongly in each spectrum and often there are even multiple histogram bars having an comparable height. Therefore, the point of the first photon stream arriving was defined to be left of the peak at 20 % of its height. In order to identify this point in time, linear interpolation between the two bars surrounding the threshold value was used.

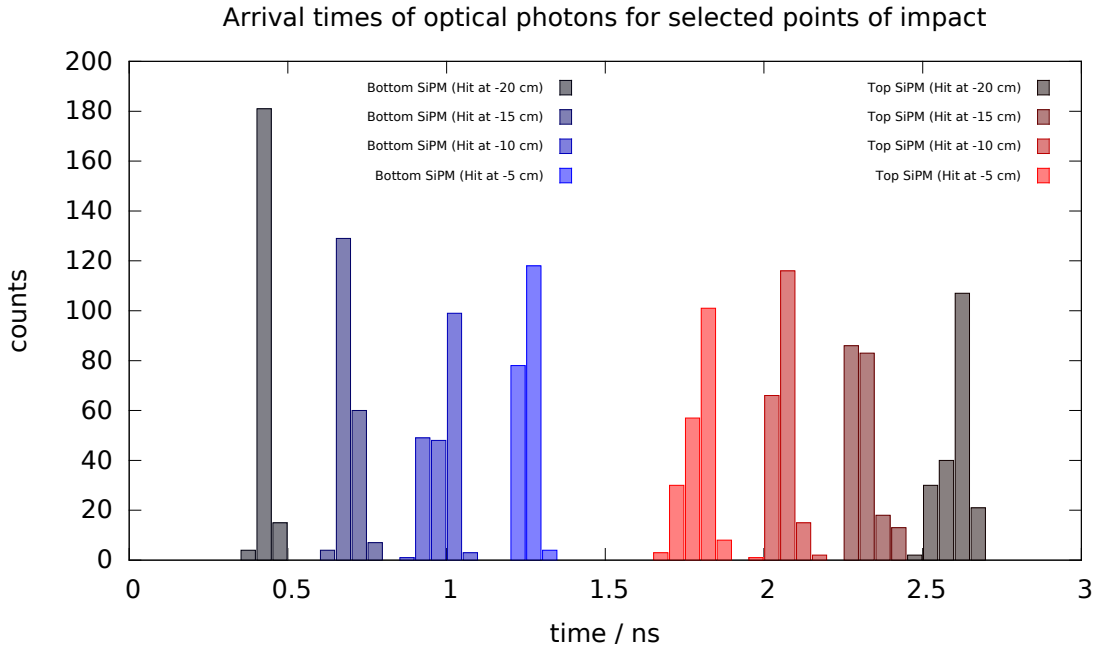

Figure 4.3: Arrival times of optical photons for selected hit points.

The obtained timestamps in each SiPM were stored for every event at a given location[4]. Figure 4.3 is a plot of timestamps of selected particle hit points. The more centered the particle strikes the scintillator, the more equal are the optical photons' times of arrival, as the plot illustrates.

Only then could the actual values of interest be calculated: Mean value, standard deviation, median, quartiles, minimum and maximum were computed using the collected timestamps in each SiPM.

After these values, for the respective position, had been stored, the procedure was repeated for every other location on the scintillator[5].

Finally, the analysis results were written into files, which were subsequently used to generate several plots visualizing the data.

4.6 Simulation Results

The results of the simulation and its analysis are best summarized by presenting them in terms of different plots.

Figure 4.4 is a box and whiskers plot of the optical photon arrival times for different positions of the initial particle hit. It basically contains the same data as figure 4.3 (only covering a wider range of hit locations) while being arranged in a different kind of plot and thus providing information more directly accessible. The height of the respective boxes represents the time interval in which 50 % of the first photonic flushes arrive for the given events. The whisker bars take up the times from the first arriving photon flush up to the time of the last one. Also delineated

[4] At this point, 400 timestamps are stored for a single point on the geometry. (400 timestamps = 200 particle hits × 2 SiPMs.)

[5] As already pointed out before, the points of impact on the scintillator are 0.1 mm apart from each other.

are medians (black lines) and mean values.

When plotting the arrival time differences between top and bottom SiPM over the location of the preceding particle hit (see figure 4.5), one gets information which is crucial for understanding the behavior of the actual scintillation detectors used in the experiment. That is the minimum uncertainty in the determination of the point of particle impact for a measured time difference, connected with corresponding probabilities.

Consequently, for a measured time interval between photon stream arrival at the top SiPM and one at the bottom SiPM, the location of the particle precedingly striking the scintillator can be pinned down to a length interval of 0.76 cm with a certainty of 50 %. However, to be (almost) perfectly certain (i.e., a certainty of estimated 99 %) of the impact location, one cannot further narrow down the length interval than 3.35 cm.

Furthermore, a box and whiskers plot showing the average time of flight of the optical photons depending on the observed time difference between top and bottom SiPM was generated (see figure 4.6). A linear fit of the medians shows a very weak dependence of the average time of flight t_{av} on the actual time difference t_{diff}, with t_{av} being about 1.51 nanoseconds. The amount of time taken by light traveling through half the scintillator in a straight line, which was calculated via the materials refractive index, is 1.19 nanoseconds. Thus, as a sideline, it can also be concluded that the photon flush which most decisively indicates a preceding particle hit mainly consists of photons having experienced several reflections on the sidewalls before reaching the end of the geometry.

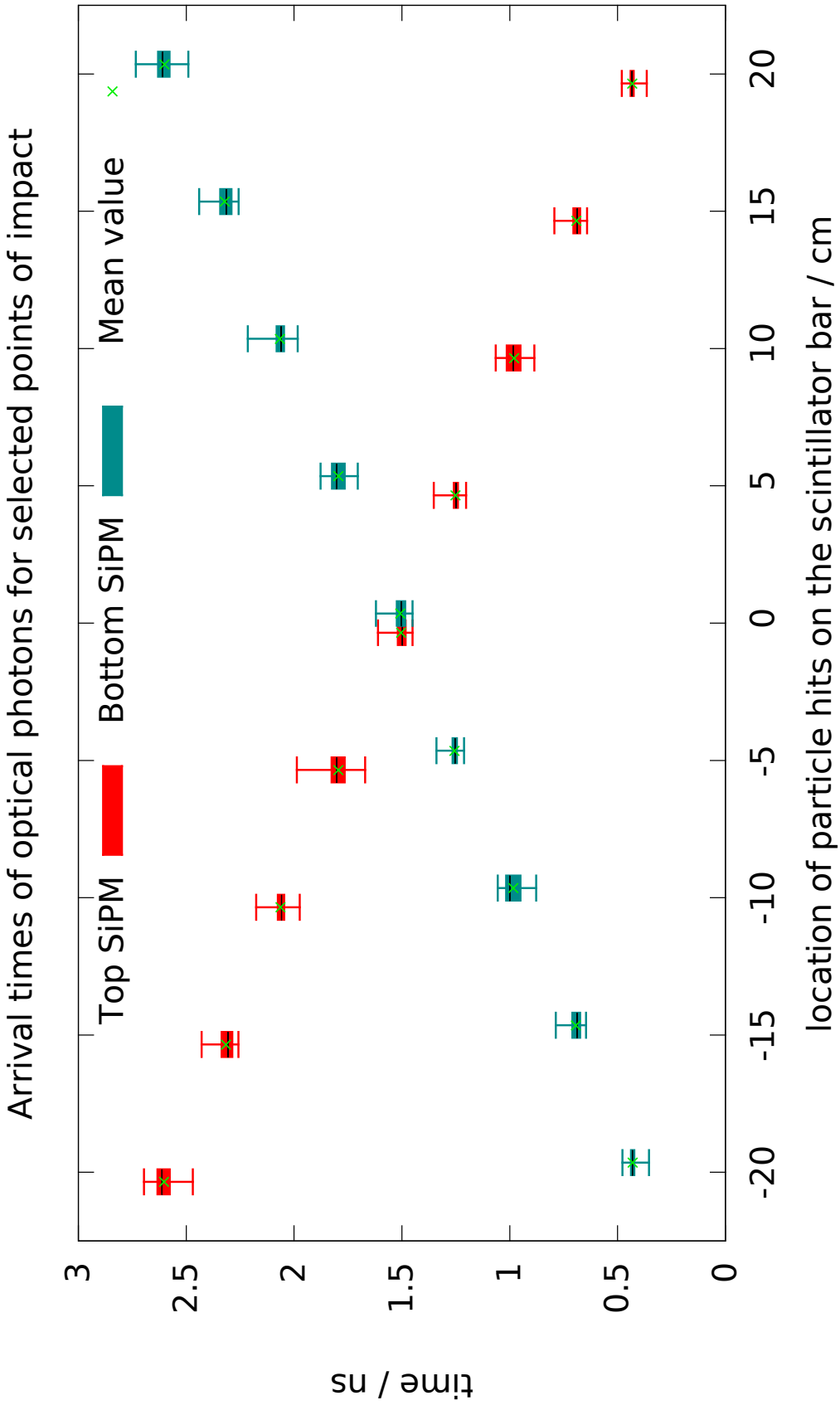

Figure 4.4: Timestamps in each SiPM pair for different points of impact.

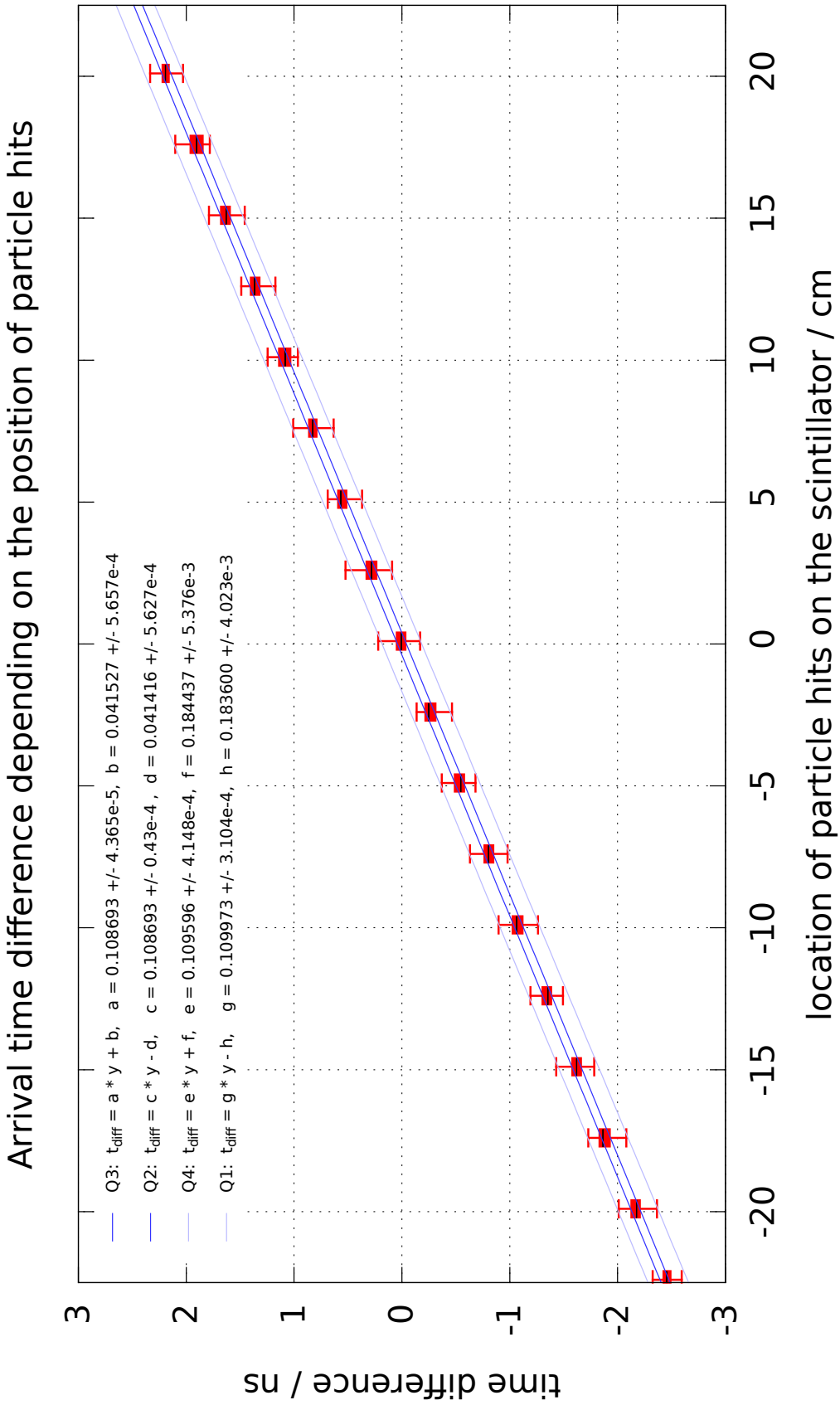

Figure 4.5: Time differences depending on the position of particle hits.

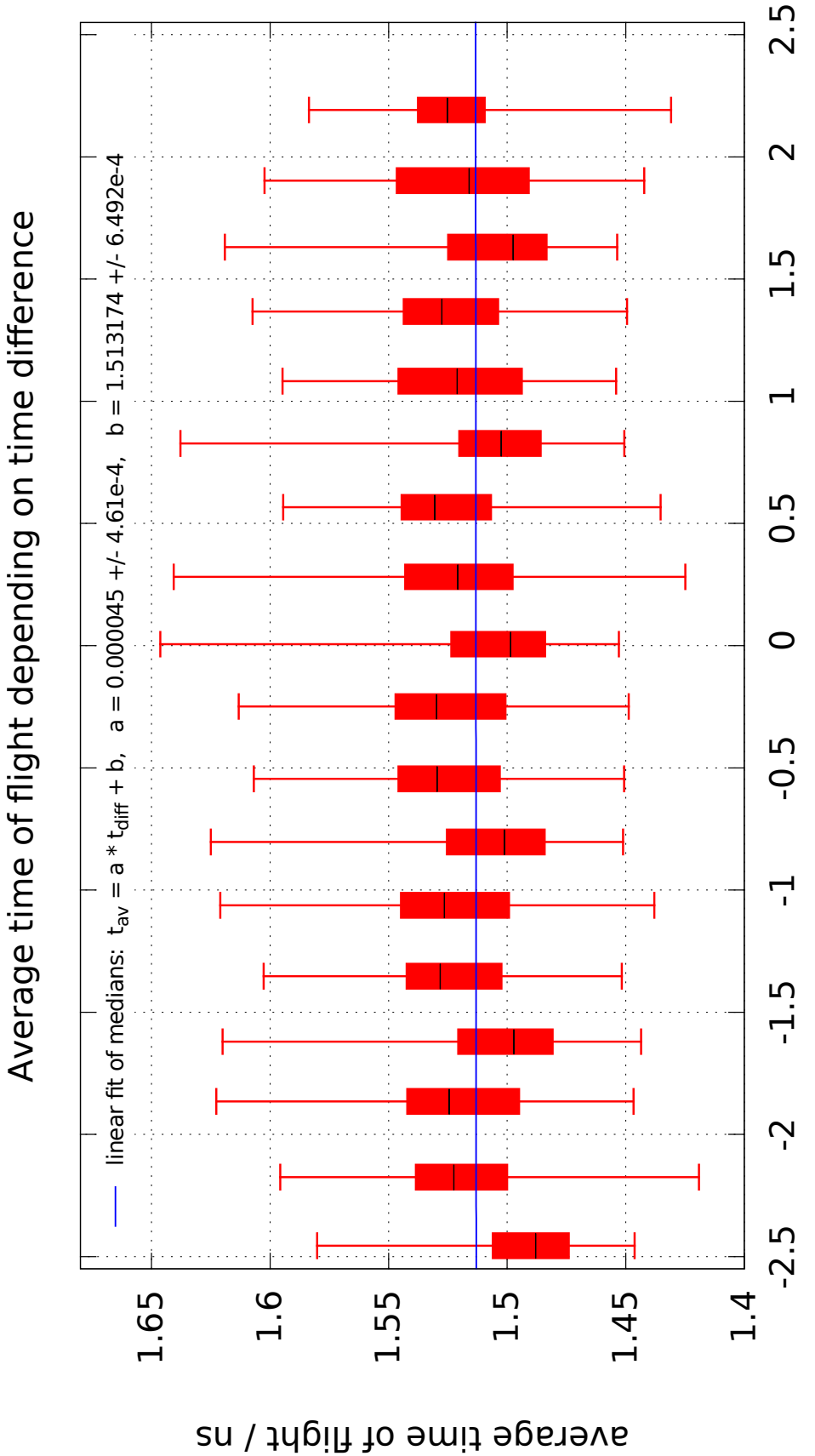

Figure 4.6: Average time of flight of optical photons depending on time difference.

Chapter 5

Summary and Outlook

The purpose of this thesis is the computation of the idealised[1] uncertainty when determining the location of a particle hit on a scintillation detector by measuring the arrival times of the optical photons at the ends of the detector geometry. The results should help in accurately understanding the behavior of the scintillation detectors used in the HBAR-GSHFS[2] experiment's CPT detector[3] by the ASACUSA[4] collaboration.

For this purpose, a simulation was programmed within the framework of the Geant4 particle physics toolkit [1, 2]. The geometry was thereby implemented by importing a pre-defined GDML[5] file [21].

In the course of the simulation run, the scintillator was rastered with a monoenergetic beam of negatively charged pions (330.8774 eV) at intervals of 0.1 mm, where 200 particles were fired at each point. The arrival time of every optical photon hitting a sensitive detector element (i.e., a SiPM pair at either end of the detector) was logged and stored.

Subsequent analysis of the time data finally resulted in meaningful predictions concerning the position resolution of an ideal scintillation detector: For any measured difference between the optical photon arrival times in one and in the other SiPM, a reconstruction of the original particle's point of impact is ideally possible within a length interval of 0.76 cm with a certainty of 50 % and within 3.35 cm with a certainty of estimated 99 % (see figure 4.5 on page 22).

Prospectively, it seems reasonable to build upon this work by also simulating and analyzing the optical photon processes in one of the smaller[6] scintillation detectors which, too, are integrated in the CPT detector.

Furthermore, in order to obtain the actual (the "real") output of the scintillation detector, it is desirable to consider the behavior of the built-in electronics as well. A logical next step would be, for example, the convolution of the simulated signal with the SiPM response function.

[1] Electronic effects and non-ideal optical coupling are neglected.
[2] "Antihydrogen ground state hyperfine splitting"
[3] "Compact Pion Tracking detector"
[4] "Atomic Spectroscopy And Collision Using Slow Antiprotons"
[5] "Geometry Description Mark-up Language"
[6] The dimensions of the smaller scintillator bars in the hodoscope are $20 \times 300 \times 5$ mm, whereas those treated in this work are $35 \times 450 \times 5$ mm.

List of Figures

List of Tables

Appendices

Appendix A

Technical Drawings

A.1 A Scintillator with Light Guides

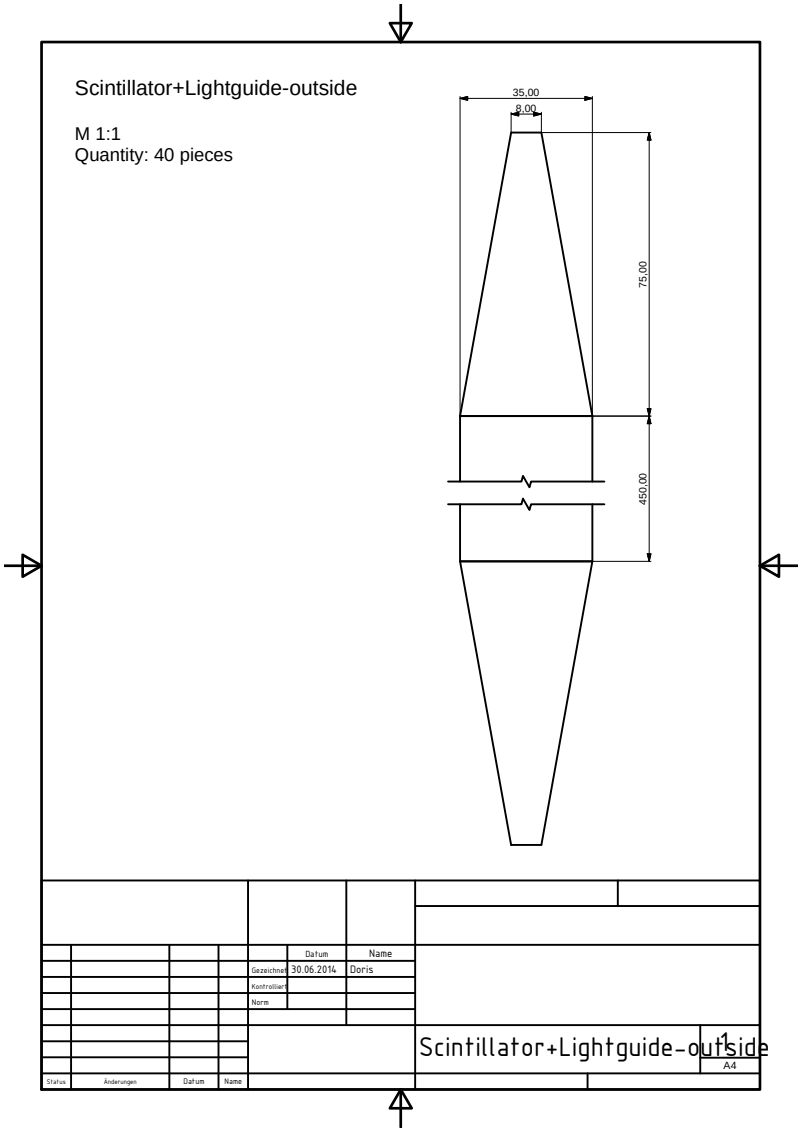

Figure A.1: Technical drawing of a scintillator with light guides as used in the simulation.

A.2 The Experimental Setup of the Beamline

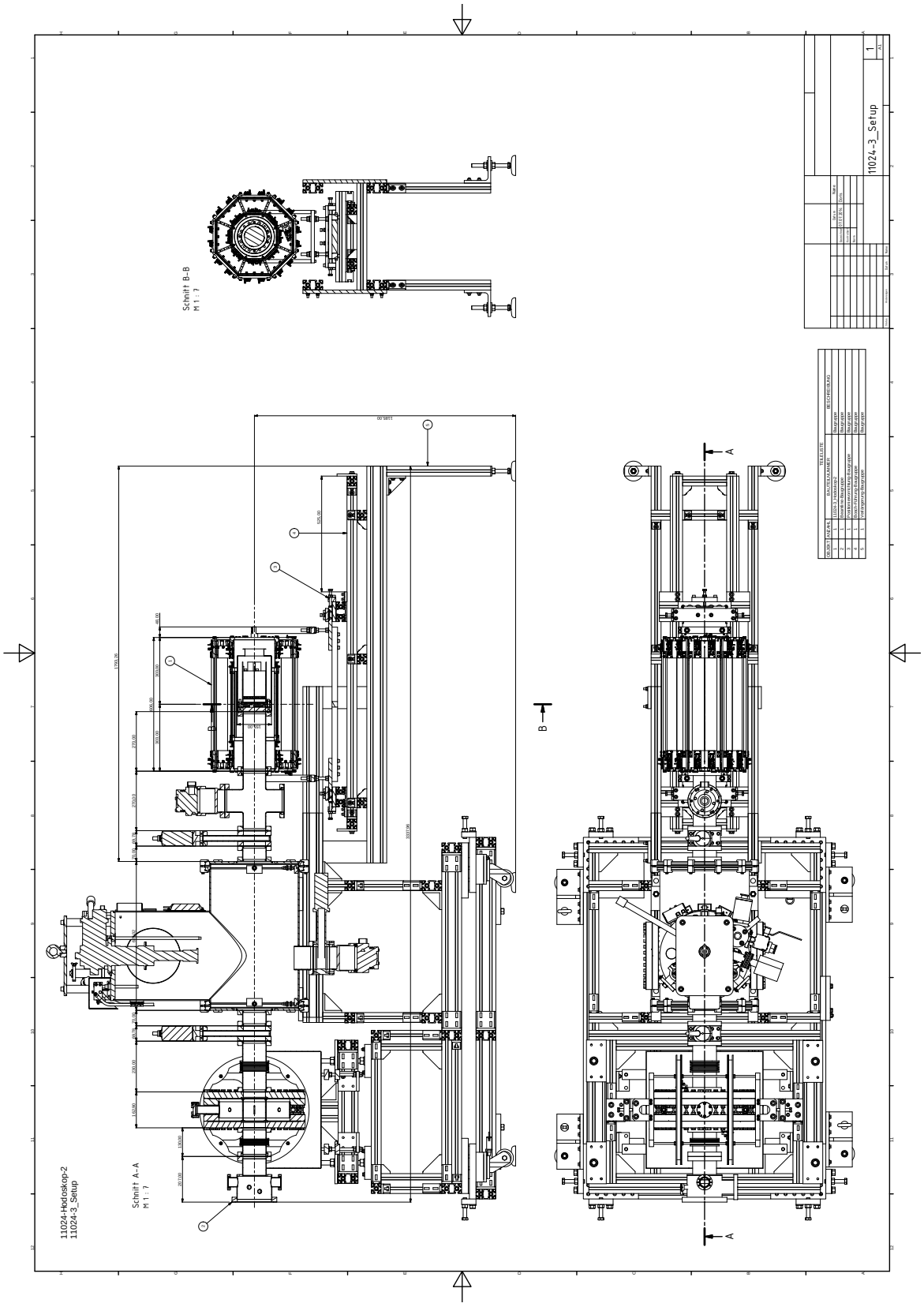

Figure A.2: Technical drawings of the experimental setup.

Appendix B

Data Plots

B.1 Refractive Index of Aluminium

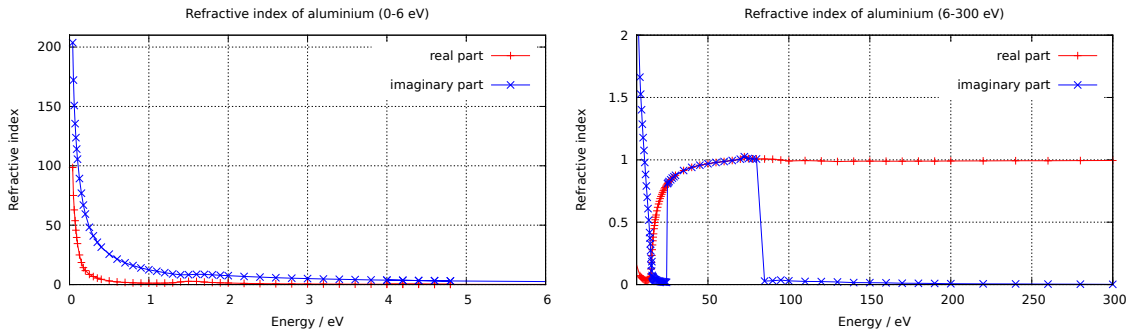

Figure B.1: Refractive index of aluminium (plotted from file data) [26, p. 327f].

B.2 Relative Light Output of the Scintillator

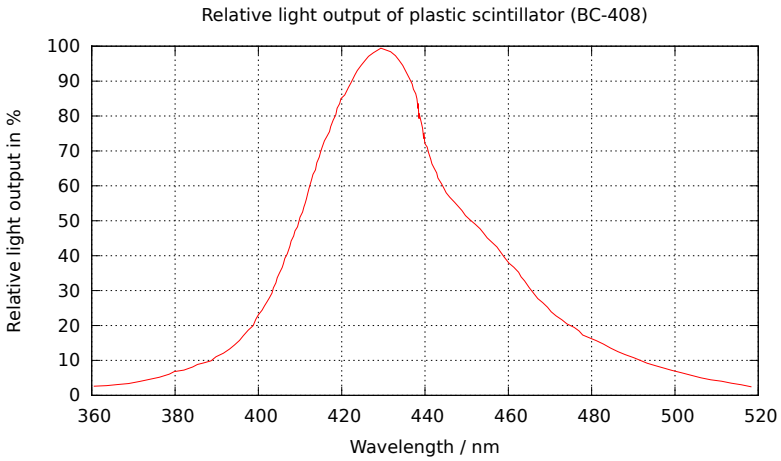

Figure B.2: Relative light output of the scintillator (plotted from file data) [25].

Appendix C

Simulation Code

C.1 Definition of Materials

File source: "include/DetectorConstruction.hh":

```
G4Material* air;
G4Material* ScintiMaterial;
G4Material* LightguidesMaterial;
G4Material* SiPMMaterial;
G4Material* WrappingMaterial;
```

File source: "src/DetectorConstruction.cc":

```
G4NistManager* Nistman = G4NistManager::Instance();
air = Nistman->FindOrBuildMaterial("G4_AIR");

G4Element* H  = new G4Element("Hydrogen", "H", 1., 1.01 *g/mole);
G4Element* C  = new G4Element("Carbon", "C", 6., 12.01 *g/mole);
G4Element* Si = new G4Element("Silicon", "Si", 14., 28.09 *g/mole);
G4Element* Al = new G4Element("Aluminium", "Al", 13., 26.98 *g/mole);

// Scintillator bar
ScintiMaterial = new G4Material("ScintillatorMaterial", 1.032 *g/cm3, 2);
ScintiMaterial->AddElement(C, 9);
ScintiMaterial->AddElement(H, 10);

// Lightguides
LightguidesMaterial = new G4Material("LightguidesMaterial", 1.032 *g/cm3, 2);
LightguidesMaterial->AddElement(C, 9);
LightguidesMaterial->AddElement(H, 10);

// SiPM
SiPMMaterial = new G4Material("SiPM", 2.33 *g/cm3, 1);
SiPMMaterial->AddElement(Si, 1.);

// Wrapping
WrappingMaterial = new G4Material("Wrapping", 2.7 *g/cm3, 1);
WrappingMaterial->AddElement(Al, 1.);
```

C.2 Optical Material Properties

C.2.1 Registering of Optical Physics in the Physics List

File source: "src/PhysicsList.cc":

```
G4OpticalPhysics * opticalPhysics = new G4OpticalPhysics();
RegisterPhysics( opticalPhysics );

// adjust parameters for optical physics
opticalPhysics->SetWLSTimeProfile("delta");
```

```
opticalPhysics->SetScintillationYieldFactor(1.0);
opticalPhysics->SetScintillationExcitationRatio(0.0);
opticalPhysics->SetMaxNumPhotonsPerStep(100);
opticalPhysics->SetMaxBetaChangePerStep(10.0);
opticalPhysics->SetTrackSecondariesFirst(kScintillation, true);
```

C.2.2 Setting Scintillation Properties for the Scintillator Material

File source: "include/DetectorConstruction.hh":

```
G4Material* ScintiMaterial;
   ...
G4MaterialPropertiesTable * Scinti_MPT;
   ...
std::vector<double> Scinti_PP;
std::vector<double> Scinti_FAST;
std::vector<double> rindex_scinti;
std::vector<double> absorption;
```

File source: "src/DetectorConstruction.cc":

```
Scinti_MPT = new G4MaterialPropertiesTable();
Scinti_MPT->AddProperty("FASTCOMPONENT", &(Scinti_PP[0]), &(Scinti_FAST[0]),
    Scinti_PP.size());
Scinti_MPT->AddConstProperty("SCINTILLATIONYIELD", 10000./MeV);
Scinti_MPT->AddConstProperty("RESOLUTIONSCALE", 1.0);
Scinti_MPT->AddConstProperty("FASTTIMECONSTANT", 1. *ns);
Scinti_MPT->AddProperty("RINDEX", &(Scinti_PP[0]), &(rindex_scinti[0]), Scinti_PP.
    size());
Scinti_MPT->AddProperty("ABSLENGTH", &(Scinti_PP[0]), &(absorption[0]), Scinti_PP.
    size());
ScintiMaterial->SetMaterialPropertiesTable(Scinti_MPT);
```

The vector `Scinti_PP` contains energy values in electron volts and `Scinti_FAST` the corresponding scintillation fast component in terms of relative light output. `rindex_scinti` holds the refractive index information and `absorption` the scintillator absorption length.

C.2.3 Setting Optical Material Properties for the Aluminium Wrapping

File source: "include/DetectorConstruction.hh":

```
std::vector<double> Al_real_PP;
std::vector<double> Al_real;
std::vector<double> Al_imag_PP;
std::vector<double> Al_imag;
```

File source: "src/DetectorConstruction.cc":

```
G4GDMLParser fParser;
fParser.Read("data/gdml/scintillator_logical.gdml", false);
   ...
G4OpticalSurface * OptSurface = new G4OpticalSurface("wrappingSurface");
G4LogicalSurface * BarWrappingSurface =
   new G4LogicalSkinSurface("bar_wrapping_surface", fParser.GetVolume("
    scinti_bar_wrapping"), OptSurface);
G4LogicalSurface * LightguideWrappingSurface =
   new G4LogicalSkinSurface("lightguide_wrapping_surface", fParser.GetVolume("
    scinti_lightguide_wrapping"), OptSurface);

OptSurface->SetType(dielectric_metal);
OptSurface->SetFinish(polished);
OptSurface->SetModel(glisur);

```

```
G4MaterialPropertiesTable * OptSurface_MPT = new G4MaterialPropertiesTable();
OptSurface_MPT->AddProperty("REALRINDEX", &(Al_real_PP[0]), &(Al_real[0]),
    Al_real_PP.size());
OptSurface_MPT->AddProperty("IMAGINARYRINDEX", &(Al_imag_PP[0]), &(Al_imag[0]),
    Al_imag_PP.size());
OptSurface->SetMaterialPropertiesTable(OptSurface_MPT);
```

The vector `Al_real` holds the real part and `Al_imag` the imaginary part of the aluminium refractive index. Both `Al_real_PP` and `Al_imag_PP` contain the corresponding energy values in electron volts.

C.3 Sensitive Detectors

C.3.1 Making the SiPMs Sensitive

File source: "include/DetectorConstruction.hh":

```
ScintillatorSD* SiPMSD_top;
ScintillatorSD* SiPMSD_bottom;
```

File source: "src/DetectorConstruction.cc":

```
// Read GDML file
G4GDMLParser fParser;
fParser.Read("data/gdml/scintillator_logical.gdml", false);
   ...
// Set SiPMs sensitive
SiPMSD_top = new ScintillatorSD("/detector/SiPM_top");
fParser.GetVolume("SiPM_top")->SetSensitiveDetector(SiPMSD_top);
G4SDManager::GetSDMpointer()->AddNewDetector(SiPMSD_top);
//
SiPMSD_bottom = new ScintillatorSD("/detector/SiPM_bottom");
fParser.GetVolume("SiPM_bottom")->SetSensitiveDetector(SiPMSD_bottom);
G4SDManager::GetSDMpointer()->AddNewDetector(SiPMSD_bottom);
```

C.3.2 Processing Hits in the SiPMs

File source: "include/ScintillatorSD.hh":

```
SiHitCollection * hitCollection;
G4Track * track;
G4int hitCounter;
G4String volName;
std::vector<G4double> SiPM_top_timeData;
std::vector<G4double> SiPM_bottom_timeData;
std::vector<G4double> SiPM_top_energyData;
std::vector<G4double> SiPM_bottom_energyData;
```

File source: "src/ScintillatorSD.cc":

```
void ScintillatorSD::Initialize(G4HCofThisEvent* HCE)
{
     ...
  hitCollection = new SiHitCollection(GetName(), collectionName[0]);

  static G4int HCID = -1;
  if (HCID<0) { HCID = GetCollectionID(0); }
  HCE->AddHitsCollection(HCID, hitCollection);
     ...
}
```

```
G4bool ScintillatorSD::ProcessHits(G4Step * step, G4TouchableHistory* )
{
  G4TouchableHandle touchable = step->GetPreStepPoint()->GetTouchableHandle();

  track = step->GetTrack();
```

```
6
7   if( step->GetPreStepPoint()->GetStepStatus() == fGeomBoundary ) {
8     G4double preTime = step->GetPreStepPoint()->GetGlobalTime();
9     track->SetTrackStatus(fKillTrackAndSecondaries);
10        ...
11    G4double time = step->GetPreStepPoint()->GetGlobalTime();
12
13    if(track->GetVolume()->GetName() == "SiPM_top")
14      {
15  SiPM_top_timeData.push_back(step->GetPreStepPoint()->GetGlobalTime());
16  SiPM_top_energyData.push_back(step->GetPreStepPoint()->GetTotalEnergy());
17      }
18    if(track->GetVolume()->GetName() == "SiPM_bottom")
19      {
20  SiPM_bottom_timeData.push_back(step->GetPreStepPoint()->GetGlobalTime());
21  SiPM_bottom_energyData.push_back(step->GetPreStepPoint()->GetTotalEnergy());
22      }
23  }
24
25  if (step->GetTotalEnergyDeposit() <= 0.) return false;
26
27  return true;
28 }
```

```
1  void ScintillatorSD::EndOfEvent(G4HCofThisEvent* HE)
2  {
3       ...
4    // Write hit data to files
5    G4String fileName;
6    if(GetName() == "SiPM_top")
7      { fileName = "data/hits/SiPM_top_hits.dat"; }
8    if(GetName() == "SiPM_bottom")
9      { fileName = "data/hits/SiPM_bottom_hits.dat"; }
10   std::ofstream fileOut(fileName);
11   if(GetName() == "SiPM_top")
12     {
13       for(std::vector<G4double>::const_iterator i = SiPM_top_timeData.begin(); i !=
      SiPM_top_timeData.end(); ++i)
14   {
15     std::vector<G4double>::const_iterator j = SiPM_top_energyData.begin();
16     fileOut << *i/ns << '\t' << *j/eV << '\n';
17     ++j;
18   }
19     }
20   if(GetName() == "SiPM_bottom")
21     {
22       for(std::vector<G4double>::const_iterator i = SiPM_bottom_timeData.begin(); i
      != SiPM_bottom_timeData.end(); ++i)
23   {
24     std::vector<G4double>::const_iterator j = SiPM_bottom_energyData.begin();
25     fileOut << *i/ns << '\t' << *j/eV << '\n';
26     ++j;
27   }
28     }
29       ...
30 }
```

Bibliography

[1] S. Agostinelli et al. Geant4—a simulation toolkit. *Nuclear Instruments and Methods in Physics Research Section A: Accelerators, Spectrometers, Detectors and Associated Equipment*, 506(3):250 – 303, 2003. ISSN 0168-9002. doi: http://dx.doi.org/10.1016/S0168-9002(03)01368-8. URL http://www.sciencedirect.com/science/article/pii/S0168900203013688.

[2] J. Allison et al. Geant4 developments and applications. *Nuclear Science, IEEE Transactions on*, 53(1):270–278, Feb 2006. ISSN 0018-9499. doi: 10.1109/TNS.2006.869826.

[3] N. Bohr. On the constitution of atoms and molecules. *Philosophical Magazine Series 6*, 26(151):1–25, 1913. doi: 10.1080/14786441308634955. URL http://dx.doi.org/10.1080/14786441308634955.

[4] Paul A. M. Dirac. The quantum theory of the electron. *Proceedings of the Royal Society of London. Series A, Containing Papers of a Mathematical and Physical Character*, pages 610–624, 1928.

[5] C. D. Anderson. The Apparent Existence of Easily Deflectable Positives. *Science*, 76:238–239, September 1932. doi: 10.1126/science.76.1967.238.

[6] J. H. Christenson, J. W. Cronin, V. L. Fitch, and R. Turlay. Evidence for the 2π decay of the k_2^0 meson. *Phys. Rev. Lett.*, 13:138–140, Jul 1964. doi: 10.1103/PhysRevLett.13.138. URL http://link.aps.org/doi/10.1103/PhysRevLett.13.138.

[7] Gerhart Lüders. On the Equivalence of Invariance under Time Reversal and under Particle-Antiparticle Conjugation for Relativistic Field Theories. *Kong.Dan.Vid.Sel.Mat.Fys.Med.*, 28N5:1–17, 1954.

[8] W. Pauli. Niels Bohr and the development of physics. *McGraw-Hill*, 1955.

[9] O. W. Greenberg. CPT Violation Implies Violation of Lorentz Invariance. *Phys. Rev. Lett.*, 89:231602, Nov 2002. doi: 10.1103/PhysRevLett.89.231602. URL http://link.aps.org/doi/10.1103/PhysRevLett.89.231602.

[10] Norman F Ramsey. Experiments with separated oscillatory fields and hydrogen masers. *Rev. Mod. Phys.*, 62:541–552, Jul 1990. doi: 10.1103/RevModPhys.62.541. URL http://link.aps.org/doi/10.1103/RevModPhys.62.541.

[11] Helmut Hellwig, Robert FC Vessot, Martin W Levine, Paul W Zitzewitz, David W Allan, and David J Glaze. Measurement of the unperturbed hydrogen hyperfine transition frequency. *Instrumentation and Measurement, IEEE Transactions on*, 19(4):200–209, 1970.

[12] B Kolbinger. Numerical simulations of hyperfine transitions in antihydrogen. Master's thesis, University of Vienna, 2014.

[13] E. Noether. Invariante Variationsprobleme. *Nachr. d. Koenigl. Gesellsch. d. Wiss. zu Goettingen, Math-phys. Klasse*, pages 235–257, 1918.

[14] A Variola, M Amoretti, G Bonomi, PD Bowe, C Carraro, CL Cesar, M Charlton, M Doser, V Filippini, A Fontana, et al. Towards cold antihydrogen spectroscopy. In *CONFERENCE PROCEEDINGS-ITALIAN PHYSICAL SOCIETY*, volume 90, page 213. Editrice Compositori; 1999, 2005.

[15] Norman F Ramsey. Experiments with trapped hydrogen atoms and neutrons. *Physica Scripta*, 1995(T59):323, 1995.

[16] Sune Svanberg. *Atomic and molecular spectroscopy: basic aspects and practical applications; with 14 tables*. Springer, 2004.

[17] Walther Gerlach and Otto Stern. Der experimentelle Nachweis der Richtungsquantelung im Magnetfeld. *Zeitschrift für Physik A Hadrons and Nuclei*, 9(1):349–352, 1922.

[18] E Widmann, M Diermaier, B Juhász, C Malbrunot, O Massiczek, C Sauerzopf, K Suzuki, B Wünschek, J Zmeskal, S Federmann, et al. Measurement of the hyperfine structure of antihydrogen in a beam. *Hyperfine Interactions*, 215(1-3): 1–8, 2013.

[19] Y. Enomoto, N. Kuroda, K. Michishio, C. H. Kim, H. Higaki, Y. Nagata, Y. Kanai, H. A. Torii, M. Corradini, M. Leali, E. Lodi-Rizzini, V. Mascagna, L. Venturelli, N. Zurlo, K. Fujii, M. Ohtsuka, K. Tanaka, H. Imao, Y. Nagashima, Y. Matsuda, B. Juhász, A. Mohri, and Y. Yamazaki. Synthesis of Cold Antihydrogen in a CUSP Trap. *Physical Review LettersPhys. Rev. Lett.*, 105:243401 –, 2010/12/07/ 2010. URL http://link.aps.org/doi/10.1103/PhysRevLett.105.243401.

[20] ASACUSA collaboration. CUSP trap experiments in ASACUSA collaboration, August 2014. URL http://radphys4.c.u-tokyo.ac.jp/musashi/node/38.

[21] Radovan Chytracek, Jeremy McCormick, Witold Pokorski, and Giovanni Santin. Geometry description markup language for physics simulation and analysis applications. *Nuclear Science, IEEE Transactions on*, 53(5):2892–2896, 2006.

[22] Rene Brun and Fons Rademakers. Root—an object oriented data analysis framework. *Nuclear Instruments and Methods in Physics Research Section A: Accelerators, Spectrometers, Detectors and Associated Equipment*, 389(1):81–86, 1997.

[23] C. M. Poole, I. Cornelius, J. V. Trapp, and C. M. Langton. A CAD Interface for GEANT4. *Australasian Physical and Engineering Science in Medicine*, September 2012. doi: 10.1007/s13246-012-0159-8. URL http://www.springerlink.com/content/u563877422284578.

[24] C. Poole, I. Cornelius, J. Trapp, and C.M. Langton. Fast tessellated solid navigation in GEANT4. *IEEE Transactions on Nuclear Science*, 99:1–7, 2012.

[25] *Premium Plastic Scintillators, BC-408 datasheet*. Saint-Gobain Crystals, 2014. URL http://www.crystals.saint-gobain.com.

[26] Marvin J Weber. *Handbook of optical materials*, volume 19. CRC press, 2002.

Danksagung

An dieser Stelle möchte ich mich bei jenen Personen bedanken, die wesentlich zum Erfolg dieser Bachelorarbeit beigetragen haben.

Mein erster Dank gilt Prof. Dr. Eberhard Widmann für die freundliche und unkomplizierte Aufnahme am Stefan-Meyer-Institut.

Weiterer Dank geht an Privatdoz. Dipl.-Ing. Dr. Johann Marton für die Beurteilung meiner Arbeit und das Übernehmen der organisatorischen Angelegenheiten.

Ganz besonders möchte ich mich bei Clemens Sauerzopf für die exzellente Betreuung während der warmen Sommermonate bedanken. Er hat mich motiviert, nicht nur jene Programme zu lernen und zu verwenden, die unmittelbar für meine Simulation erforderlich waren, sondern auch welche, die für eine eventuelle spätere (Mit-)Entwicklung von Programmen von großem Nutzen sein werden. Seine Geduld und sein entgegengebrachtes Verständnis beim Beantworten meiner zahlreichen Fragen sowie das Aufrechterhalten einer lockeren und unterhaltsamen Atmosphäre habe ich immer sehr geschätzt.

Großen Dank möchte ich auch Aaron Capon aussprechen, der sich bereit erklärt hat, meinen Text durchzugehen, und einen großen Beitrag zu dessen Leserlichkeit geleistet hat. *Thanks Aaron, I really appreciate it! You were of great help.*

Danke außerdem an das gesamte SMI-Team für die selbstverständlich wirkende Miteinbeziehung am Institut, für all die gemütlichen Mittagspausen und für das eine oder andere gemeinsame Bier am Ende eines Arbeitstages. Es hat mir Spaß gemacht, mit euch zu arbeiten.

Nicht unerwähnt bleiben dürfen Lukas Lechner und Magdalena Haselsteiner, zwei meiner besten Freunde, die mir hilfreiche Tipps zum Verfassen dieser Arbeit gegeben haben. Ebenso möchte ich mich aber auch bei all meinen anderen Studienkollegen für den Zusammenhalt und die Freundschaft bedanken, die wesentlich dazu beitragen, dass ich mein Studium mit immer noch so großer Motivation angehe.

Der größte Dank gilt allerdings meiner Familie für die andauernde und bedingungslose Unterstützung meiner Tätigkeiten, ohne die mein Alltag nicht derart sorgenfrei und für mich interessant sein könnte.